Direct visualization of colloid transport over natural heterogeneous and artificial smooth rock surfaces

Oshri Borgman, Avraham Be'Er, Noam Weisbrod

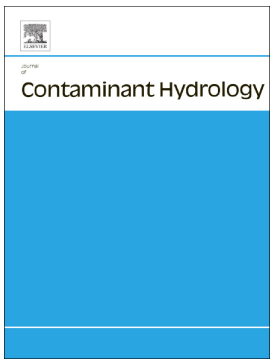

Direct visualization of colloid transport over natural heterogeneous and artificial smooth rock surfaces

Oshri Borgman, Avraham Be'er, Noam Weisbrod

PII: S0169-7722(22)00115-2

DOI: https://doi.org/10.1016/j.jconhyd.2022.104067

Reference: CONHYD 104067

To appear in: *Journal of Contaminant Hydrology*

Received date: 11 March 2022

Revised date: 13 August 2022

Accepted date: 28 August 2022

Please cite this article as: O. Borgman, A. Be'er and N. Weisbrod, Direct visualization of colloid transport over natural heterogeneous and artificial smooth rock surfaces, *Journal of Contaminant Hydrology* (2022), https://doi.org/10.1016/j.jconhyd.2022.104067

Direct visualization of colloid transport over natural heterogeneous and artificial smooth rock surfaces

Oshri Borgman[1,2,*] oshri.borgman@mail.huji.ac.il, Avraham Be'er[1], Noam Weisbrod[1]

[1]Zuckerberg Institute for Water Research, Jacob Blaustein Institutes for Desert Research, Ben-Gurion University of the Negev, Midreshet Ben-Gurion 8499000, Israel

[2]Univ Rennes, CNRS, Géosciences Rennes, UMR 6118, 35000, Rennes, France

[*]Corresponding author.

Abstract

Colloid transport in fractured rock formations is an important process impacting the fate of pollutants in the subsurface. Despite intensive and outstanding research on their transport phenomena, the impact of small-scale surface heterogeneity on colloid behavior at the fracture scale remains difficult to assess. In particular, there is relatively little direct experimental evidence on the impact of natural fracture surface heterogeneity on colloid transport. To investigate this, we developed an experimental setup allowing the direct visualization of fluorescent colloid transport in a flow cell containing a natural chalk rock sample while simultaneously monitoring effluent colloid concentrations. We used samples containing both a natural fracture surface and an artificially made smooth surface from the same chalk core. We characterized the roughness and chemical composition of both surface types and numerically calculated each surface's velocity field. From the experiments, we obtained direct images of colloid transport over the surfaces, from which we calculated their dispersion coefficients and quantified the residual deposition of colloids on the rock surface. We also measured the colloid breakthrough curves by collecting eluent samples from the flow cell outlet. The natural fracture surface exhibited larger physical and chemical heterogeneity than the smooth, artificially generated surface. The aperture variability across the natural surface led to preferential flow and colloid transport which was qualitatively apparent in the fluorescent images. The colloid transport patterns matched the calculated velocity fields well, directly linking the surface topography and aperture variation to colloid transport. Compared to the artificially made surface, the natural surface also showed higher dispersion coefficients, which corresponded to the colloids' earlier breakthrough from the flow

cell. While we found differences between the elemental composition of the natural and artificially smooth surfaces, we could not observe their impact on the colloids' surface attachment and retention. The main novelty in this work is the coupling of direct colloid transport imaging, breakthrough curve measurements, and colloid surface deposition analyses, in a flow cell containing a natural carbonate rock sample. Our experimental setup can be used to further investigate the link between surface heterogeneity, both chemical and physical, and colloid transport and deposition in natural rock fractures.

Keywords

Colloid transport; Fractured rock; Heterogeneity; Fluorescence images; Dispersion

1 Introduction

The fate of solutes and pollutants in the environment is highly dependent on their ability to migrate from their source point to other locations, where they might have undesirable effects. Fractured rock formations are ubiquitous in the subsurface and may potentially function as favorable conduits for solutes and pollutants due to the formation of highly permeable and extensive fracture networks (Sahimi, 2011). The importance of flow and transport in fracture networks is even greater in rock formations with low matrix permeability, such as the chalk formation found in southern Israel's Negev Desert (Weisbrod et al., 1999). In such conditions, fractures are effectively the only conduits for water and solutes within the rock formation (Nativ et al., 1999; Tran et al., 2020).

Colloid and colloid-facilitated contaminant transport in fractured rock are highly relevant to environmental transport processes. During colloid-facilitated transport, soluble pollutants are attached to (or form) colloids, which in turn can migrate great distances over short time periods. This phenomenon has long been identified as a mechanism for enhanced pollutant transport in the environment (McCarthy & Zachara, 1989). Colloid-facilitated transport is also specifically linked to the enhanced migration of radionuclides from nuclear test sites (Kersting et al., 1999; Zavarin et al., 2013), constituting a major concern for the environmental safety of subsurface nuclear waste repositories (Missana et al., 2008; Albarran et al., 2013). The transport phenomena of the colloids themselves are also important on their own, for example, in the transport of bacteria and viruses to the groundwater (Weisbrod et al., 2013) or the

migration of the now ubiquitous microplastics (Horton & Dixon, 2018; Brewer et al., 2021).

Predicting flow and transport in fractured media remains an outstanding challenge, in part by the need to upscale flow and transport from the single fracture scale to the fracture network (Berre et al., 2019). In heterogeneous fracture networks, the impact of small-scale features and single fractures might be more significant (Kang et al., 2015). In addition, when considering reactive transport processes, it is well established that incomplete mixing at microscopic length scales can impact reaction rates at larger scales (Gramling et al., 2002; de Anna et al., 2014; Valocchi et al., 2019). Recently it was shown how wall roughness could affect bimolecular reaction rates in a channel flow, representing a longitudinal cross-section of a single fracture (Yoon & Kang, 2021). Thus, a faithful description of transport processes in single rough fractures is necessary for large-scale modeling.

The surface of rock fractures is characterized by irregular roughness at the microscale, i.e., the length scale between several micrometers and one millimeter. This roughness impacts the aperture and permeability at the single fracture scale and may also affect the flow characteristics at the fracture network scale (Méheust & Schmittbuhl, 2001; Berkowitz, 2002, Bodin et al., 2003). Larger variations of flow velocities characterize rough fracture surfaces compared to a simplistic parallel plate model of fracture permeability (Huber et al., 2012). Another important consequence of surface roughness is that the hydraulic aperture, representing the fracture's flow behavior, can be smaller than the mechanical aperture, which describes the fracture geometry (Noiriel et al., 2007; Zimmerman & Bodvarsson, 1996). In addition, varying flow orientation with respect to the (anisotropic) fracture aperture field greatly impacts liquid fluxes in the fracture (Méheust & Schmittbuhl, 2001).

Fracture flow characteristics have crucial implications for transport processes. One important result is flow channeling when the solution flows mostly through the more permeable regions of the fracture aperture, thereby significantly enhancing solute transport in fractured media (Tsang & Neretnieks, 1998; Brown et al., 1998). Experiments and models of solute transport in granite fractures have directly shown the importance of characterizing fracture surface roughness for solute transport modeling. A simplified model, which did not consider the surface roughness, did not describe well the experimentally obtained solute breakthrough curves (Stoll et al., 2019). In the context of colloid transport, the anisotropic distribution of fracture

apertures in the mean flow direction (i.e., longer correlation length of apertures in the general flow direction) has been shown to increase the dispersion of low-density particles (Chrysikopoulos & James, 2003; Boutt et al., 2006). Flow direction was also shown to dramatically impact colloid breakthrough curves in laboratory-scale experiments with granite blocks containing rough fractures, emphasizing the impact of fracture surface anisotropy (Vilks & Bachinski, 1996). In addition, it was shown that nanoscale roughness could impact colloid retention on surfaces by decreasing the electrostatically attractive collector surfaces' efficiency while increasing the efficiency of repulsive collector surfaces (Rasmuson et al., 2017). While the decrease in attractive surface efficiency was mostly attributed to the hydrodynamic effects of the flow in the boundary layer over the rough surface, the sources for the increase in the repulsive surface efficiency are still unclear (Jin et al., 2015; Rasmuson et al., 2019).

Fracture surfaces also exhibit chemical heterogeneity due to their diverse mineral composition. Typically, they are partially coated by deposited material, resulting from long-term flow and transport processes along the surfaces (Thoma et al., 1992; Weisbrod et al., 2000, Noiriel et al., 2007). These deposits may include metal oxides, precipitated salts, and clay minerals, and thus, they may alter the characteristics of the fracture surface with relation to the bulk rock matrix (Weisbrod et al., 1999). Nevertheless, the surface chemical or mineralogical composition effects on colloid retention remain unclear. It was found that colloid retention and deposition on fracture surfaces can occur under both electrostatically repulsive (unfavorable) and attractive (favorable) conditions, for rock fracture (Alonso et al., 2009; Albarran et al., 2013; Spanik et al., 2021) and rough glass (Rasmuson et al., 2019; Ron & Johnson, 2020) surfaces. In some cases, it was impossible to establish a correlation between the presence of specific minerals on the surface and colloid deposition (Chinju et al., 2001; Albarran et al., 2013).

Several studies have used artificially cut and sometimes polished fracture surfaces in colloid transport experiments (Chinju et al., 2001; Zavarin et al., 2013; Albarran et al., 2013). Stoll et al. (2016) shown that in colloid transport experiments in a flow cell with two surface types (a natural rock sample and an acrylic surface), the surface roughness plays an important role in colloid retention. In some studies, a new fracture is created in a solid rock block (Spanik et al., 2021). However, flow-through experiments have shown that fracture surfaces can evolve physically and chemically as they are weathered by environmental flow processes (Weisbrod et al., 2000; Noiriel

et al., 2007). While temporal changes in fracture surface heterogeneity were not examined here, the aforementioned findings emphasize the need to use natural fracture surfaces to correctly estimate their transport properties.

In most studies, the qualitative and quantitative analyses of colloid transport behavior were mostly based on breakthrough curve measurements and analyses, and the colloid retention and deposition patterns were based on post-experimental analyses of the rock surface. Rodrigues and Dickson (2015) presented a hybrid approach, using naturally fractured rock samples and their transparent acrylic replicas to study bacterial transport. Their comparison of the breakthrough curves of the natural and transparent synthetic fractures demonstrated the impact of fracture surface material on bacterial retention. The transparent fractures demonstrated preferential bacterial transport. Therefore, the coupling of both transport dynamics and overall transport behavior for natural fracture samples remains a challenge.

In many previous works, crystalline rocks were used as the fractured media due to their relevance to specific countries and locations (Albarran et al., 2013; Stoll et al., 2016). However, carbonate rocks are also important media for contaminant transport in many cases (Froidevaux et al., 2010; Mondal & Sleep, 2012; Medici et al., 2019). For example, sedimentary rock and, specifically, chalk are common in subsurface formations in southern Israel's Negev Desert. It was shown that fractures play a major role in these formations and facilitate contaminant and colloid transport (Zvikelsky & Weisbrod, 2006; Kurtzman et al., 2007; Tang & Weisbrod, 2010; Cohen & Weisbrod, 2018; Tran et al., 2020). The chemical and mineralogical compositions of the fracture surface can be important factors in determining colloid deposition behavior (Trauscht et al., 2015), and ζ-potentials can vary significantly between different rock types (Ishido & Muzutani, 1981). Therefore, it is of great interest to use this type of rock in colloid and contaminant transport studies to better understand and predict the behavior at the regional scale.

Here, we study the impact of fracture surface heterogeneity on colloid transport, breakthrough, and deposition, in an experimental setup that includes a naturally fractured rock surface. The goal is to simultaneously observe colloid transport and deposition by direct visualization and compare it with the overall transport behavior shown by their breakthrough curves in the same experimental flow cell. Our direct visualization technique allows us to quantify the colloids' dispersion during transport and their final deposition on the rock surface. The coupling of these observations in a

natural rock sample, and specifically in a carbonate rock, is the main novelty of this work. Our results show the direct link between fracture surface topography, flow channeling, preferential colloid transport, and their breakthrough behavior with natural rock fracture surfaces.

2 Methods

2.1 Colloid transport experiments

2.1.1 Experimental setup

We used a unique experimental system comprising a natural chalk sample encased in a flow cell with a transparent glass top cover. We mounted the flow cell on the stage of an AXIO Zoom.V16 fluorescence microscope (Carl Zeiss Microscopy, Jena, Germany), equipped with a PlanNeoFluar Z objective, an HXP 120 V light source, and an Axiocam 506 monochrome camera (Fig. 1). The flow cell's inlet was connected to the background solution bottle and to another vial containing the colloid suspension (in the same background solution). A stopcock was used to switch between the colloid suspension and the background solution, which are described in Section 2.1.3 below. The flow cell's outlet was connected to a peristaltic pump (Gilson Minipuls 3, Middleton, WI, USA), which drew liquid at a constant rate. The peristaltic pump was connected to a fraction collector (Spectra/Chrom CF-1, Houston, TX, USA), which collected eluent samples at fixed time intervals.

The body of our custom-designed flow cell was 3D-printed in Polyamide 12 nylon (Shapeways NL, Eindhoven, The Netherlands) and contained a rectangular cavity to hold the rock sample. The flow cell cover consisted of a 3D-printed Polyamide 12 nylon frame with a niche to hold the glass plate. The plastic frame was attached on top of the flow cell body with screws to hold the glass plate above the rock surface. The horizontal position of the glass plate over the flow cell's bottom section was ensured by the accuracy of the 3-D printing process. Thus, the glass did not touch the rock surface, and the flow field was continuous over it, with no dead-ends or trapped zones. Two holes were drilled into the glass to insert inlet and outlet tubes for colloid suspension and background solution. The full rock sample cavity dimensions were 70, 36, and 20 mm in length, width, and depth, respectively (Fig. 1(b)). The actual rock sample size was then slightly reduced to fit the cavity. Polydimethylsiloxane (PDMS, Polymer-G, Gvulot, Israel) was used to fill the small gap between the rock sample and the flow cell cavity and to hold the sample in place. The entire artificial fracture, including the inlet and outlet channels, had a length and width of 136 and 40 mm,

respectively. The depth of the inlet and outlet channels was 1.1 mm below the glass cover.

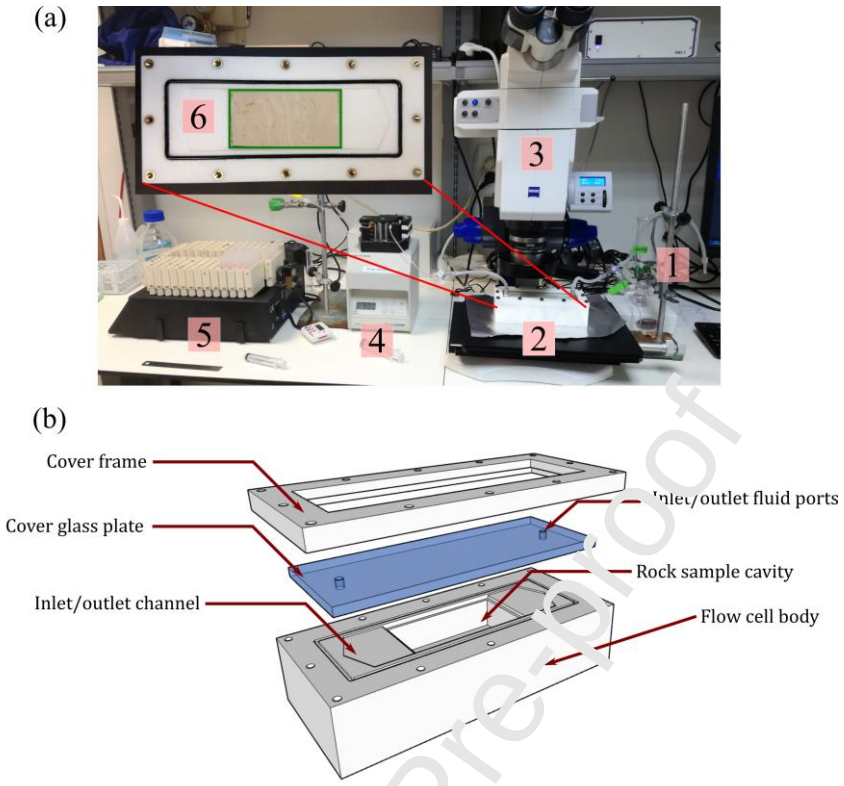

Figure 1. *(a) The experimental setup included: (1) a pulse suspension and wash solution; (2) a flow cell; (3) a fluorescence microscope; (4) a peristaltic pump; and (5) a fraction collector. (6) A top-view close-up of the flow cell showing the chalk sample in the green frame. (b) A sketch of the flow cell construction, including the three main parts – the cell body, the cover glass plate, and the plastic cover frame. The rock sample is fixed in the cavity within the cell body. The cover glass is fitted inside a niche in the cover frame, which is fixed to the cell body. This way, the glass plate's bottom side is level with the upper side of the cell body and does not touch the rock surface.*

All rock samples were cut to fit the 3-D printed flow cell's cavity so that the rock surface was exposed and a half-fracture was formed between the rock surface and the cell's glass cover. We note that in this manner, we were unable to reproduce the complete structure of a natural fracture with its two opposing rough walls. More specifically, we did not create zero-aperture points where the rock surface met the glass cover plate in our system. However, our setup still enabled us to represent the natural fracture roughness in a transparent flow cell, which allowed direct fluorescence imaging. This type of setup might be relevant to fracture apertures with a small gradient in aperture values and, thus, a small amplitude in the fracture aperture's centerline waviness.

*2.1.2 **Natural rock samples***

We used rock samples taken from coreholes drilled into the Avdat Group chalk formation in Israel's central Negev Desert (Nativ et al., 1999). Some cores were recovered as intact cylinders, while others were naturally fractured. We separated the two parts of the fractured core from the naturally fractured core samples and kept one of them to be used as a fracture surface for transport experiments. We used non-fractured cores to artificially prepare rock surfaces that were not physically or chemically altered by mechanical processes or groundwater flow. The surfaces of the naturally fractured rock samples were characterized by a large variation in surface topography and mineral deposition, which we described as having high heterogeneity (HH). The artificially created rock surface was characterized by low heterogeneity (LH), both physically and chemically (Fig. 2(a)).

We measured the surface topography of the rock samples using an Olympus LEXT OLS5000 3D scanning laser microscope (Olympus, Japan). We obtained spatial resolutions of 10, 10, and 0.1 μm in the x, y, and z coordinates, respectively. We transformed the measured elevation levels of the rock surface to the apertures of the experimental fracture cell—the vertical distances between the rock surface and the glass cover. We achieved this by measuring the distance between the bottom of the glass cover and the rock surface at a specific location. We then used this point as a reference and transformed the elevation field to a map of fracture apertures. Experiments and surface topography scanning were performed over balanced microscope stands; thus, the determination of the fracture apertures should be accurate. We calculated the relative fracture apertures over the rock surfaces, and we present them in Fig. 2(b). The relative aperture is calculated as $d(x,y) - b$, where $d(x,y)$ [L] and b [L] are the local and average apertures, respectively. The average, minimum, and maximum absolute apertures were 1.50, 1.46, and 1.57 mm for the LH sample and 0.94, 0.86, and 1.10 mm for the HH sample, respectively. We note that the fracture aperture values presented here were higher than some previously reported values in the literature, but they were still within an acceptable range. Several previous studies on fracture flow and transport have reported similar or even larger aperture values (e.g., Hu et al., 2019; Neuweiler et al., 2004; Wang & Cardenas, 2014).

To quantify the topography of the rock surface, we used standard measures of surface roughness. The arithmetic mean roughness was calculated as (Kurra et al., 2015)

$$\mathrm{Ra} = \frac{1}{n_\mathrm{p}} \sum_{i=1}^{n_\mathrm{p}} |z(i) - \overline{z}|, \quad 1)$$

where n_p is the number of pixels in the image of the surface. $z(i)$ and $\overline{z}$ are the elevation of a single pixel and the average elevation, respectively. The root mean squared roughness was calculated as (Stoll et al., 2016)

$$\mathrm{Rq} = \sqrt{\frac{1}{n_\mathrm{p}} \sum_{i=1}^{n_p} (z(i) - \overline{z})^2}. \quad 2)$$

Higher Ra values indicate a higher average difference between the surface height values and their mean, while higher Rq values indicate a wider distribution. It is important to note that the roughness characterization of our sample could not capture the nanoscale roughness structure. However, our focus here was on the characterization of a sample with an area of ~2500 mm², which makes characterizing the nanoscale roughness more challenging. At this scale, it is possible to relate colloid dispersion to surface topography and fracture aperture variations, which is difficult to quantify in nanoscale systems.

To characterize the mineralogical composition of the rock surface, we used a Quanta 200 scanning electron microscope (SEM; FEI, USA) to perform an Energy Dispersive Spectroscopy (EDS) elemental analysis of small samples from both rock surfaces. The EDS analysis was performed in areas that seemed to be of interest from visual inspection of the surfaces—for example, the black-colored regions outlined in yellow in the HH sample image in Fig. 2(a). Analyses were also performed for samples from artificially created surfaces to study the bulk rock composition. The results of these analyses are discussed in Section 3.4.

2.1.3 Background solution and colloid suspension

We used a background solution of 10 mM NaCl in deionized water throughout the experiments, with an electrical conductivity and a pH of 1.5 mS/cm and 7.1, respectively. The solution was not buffered, but measurements of eluent samples showed very small variations from the initial values (6.9 and 7.15 for the HH and LH samples, respectively). To prepare the colloid suspensions, we added 10 mg/L of orange fluorescent F-8820 FluoSpheres® carboxylate modified latex microspheres to the background solution, with a 1-µm nominal bead diameter (Molecular Probes,

USA). Their maximum excitation and emission wavelengths are 540 and 560 nm, respectively. Fresh suspensions were made for each experiment from a 1-g/L stock and transferred to a 20-ml vial placed on a magnetic stirrer 30 min before the injection into the flow cell. The addition of colloids did not change the solution's electrical conductivity or pH.

*2.1.4 **Experimental protocol***

All rock samples were saturated and equilibrated with the background solution (see Section 2.1.3) for at least 14 hours, before each experiment. In addition, at the beginning of each transport experiment, we passed several fracture aperture volumes of the background solution through the flow cell to equilibrate the surface with the solution at a flow rate of 0.1 ± 0.01 cm^3/min. This flow rate was maintained throughout the experiment, and the resulting average flow velocities varied from 0.150–0.293 cm/min (see Table 1 for details). While the mean velocities varied slightly between the experiments, the Péclet numbers (see Section 2.2.1 below and Table 1) were almost the same and did not have a clear trend depending on the type of rock surface. In addition, our experimental results showed that the variation in surface topography between the samples made the most significant impact on colloid transport.

A typical transport experiment included two stages: (1) a colloid suspension pulse of between 2.3 and 2.9 fracture aperture volumes at a constant concentration was injected into the flow cell; and (2) the flow cell was washed with the background solution until the surface fluorescence did not change, indicating that deposited colloids could not be removed under the prevalent flow conditions.

During each experiment, we collected fluorescence images using the AXIO Zoom microscope. To obtain a complete image of the rock surface, we collected a panorama composed of 15 tiles (5 × 3, length × width). The size of each tile was 15.31 × 13.88 mm^2 or 2360 × 2140 pixels (length × width), with a pixel size of 6.486 × 6.486 μm^2. Thus, the spatial surface resolution of the topography characterization (see Section 2.1) was similar to that of the microscope images. Since the microscope was equipped with a manually driven stage, such acquisition typically took ~5 min to complete. The main acquisition parameters of the microscope were excitation filter wavelengths of 540–552 nm, emission filter wavelengths of 575–640 nm, a beam splitter wavelength of 560 nm, and an exposure time of 500 milliseconds.

We performed two experiments with low heterogeneity samples (experiments LH and LH-b) where we used, for each experiment, a newly prepared artificially created rock surface. For the high heterogeneity experiments (experiments HH and HH-b), we used the same rock sample and reversed the flow direction between experiments. For the latter case, we thoroughly washed the flow cell after the first experiment to remove residual fluorescence from deposited colloids. To achieve that, we flushed the rock surface (without the cover) with water and then took images of the surface to detect residual fluorescence. We repeated the washing procedure until we could not detect residual fluorescence on the rock surface. The colloids we used in our experiment had a very strong fluorescence intensity, and at low concentrations and high magnification, we could observe single colloids on the rock surface. Therefore, while we could not use a different method to verify that the entire colloid mass was completely removed from the surface, we are certain that the washing procedure described above provided us with a clean fracture surface for the following experiment.

2.2 Flow and transport characterization

2.2.1 Dimensionless numbers and the diffusion coefficient

We calculated the dimensionless Péclet (Pe) and Reynolds (Re) to characterize the flow. Pe quantifies the ratio between the diffusion and advection characteristic time scales. For large Pe, the diffusion time scale is much longer than the advection time scale, and the transport and dispersion of particles will be determined by advection within the flow field. Re represents the ratio between inertial and viscous forces within a fluid, with low Re (dominant viscous forces) leading to laminar flow. These numbers are defined here as

$$\mathrm{Pe} = \frac{\overline{u} b}{D_0} \quad (3)$$

and

$$\mathrm{Re} = \frac{\rho \overline{u} b}{\eta}. \quad (4)$$

Here, $\overline{u}$ [LT^{-1}] is the mean flow velocity in the fracture, b [L] is the typical fracture aperture, D_0 [L^{2}T^{-1}] is the colloid diffusion coefficient, ρ [ML^{-3}] is the water density, and η [ML^{-1}T^{-1}] is the dynamic viscosity. D_0 was estimated using the Stokes-Einstein equation (Bird et al. 2002)

$$D_0 = \frac{k_B T}{3\pi\eta d_p}, \quad 5)$$

where $k_B = 1.38 \times 10^{-23}$ m² kg s⁻² K⁻¹ is the Boltzmann constant, $T = 295$ K is the temperature, and $d_p = 1 \times 10^{-6}$ m is the colloid diameter. Taking η = 0.001 Pa s, we find that $D_0 = 4.32 \times 10^{-13}$ m² s.

The calculated values of Pe and Re are given in Table 1. They show that the flow in our experiment was laminar and colloid transport was advection-dominated.

2.2.2 Numerical flow simulations

The liquid velocity field over a rough surface can be computed by applying the local cubic law for every point with local aperture $d(x,y)$ on the fracture surface (Méheust & Schmittbuhl 2001),

$$\boldsymbol{q} = -\frac{d(x,y)^3}{12\eta}\boldsymbol{\nabla P}, \quad 6)$$

where $\boldsymbol{q}$ [LT⁻¹] is the local flux vector, which is equivalent to the velocity under incompressible flow conditions (Klepikova et al. 2021), and $\boldsymbol{\nabla P}$ [MT²L⁻²] is the local pressure gradient. We used COMSOL Multiphysics® to calculate the two-dimensional velocity field over the rock surface. For the COMSOL solution, the local transmissivity $T_s(x,y)$ [L²T⁻¹] of the fracture is defined as

$$T_s(x,y) = d(x,y)K_s = \frac{\rho g}{12\eta} d(x,y)^3, \quad 7)$$

where K_s is the (saturated) hydraulic conductivity [LT⁻¹], ρ [ML⁻³] is the liquid density, and g [LT⁻²] is the gravity acceleration. The local discharge per unit of fracture width (in [L²T⁻¹]) is expressed as

$$\hat{Q} = T_s|\nabla H|, \quad 8)$$

where ∇H is the local hydraulic head gradient [-]. This leads to the Reynolds equation

$$\nabla(-T_s \nabla H) = 0, \quad 9)$$

which is solved for both topographies. We applied a constant atmospheric head boundary condition (H=0 mm) on the inlet boundary and a constant flux boundary condition on the outlet boundary to match the experimental conditions. The flux

boundary condition was given as the flow rate per unit width of the flow cell, which was 0.025 cm/min. We used in the simulations ρ = 1000 kg m^3 and η = 0.001 Pa s since the addition of salt to the solution (see Section 2.1.3) did not affect these values significantly. From the numerical solution, we calculated the velocity magnitude $U(x,y) = \sqrt{u^2 + v^2}$ [L/T], with u and v as the local velocities in the x and y directions (along and perpendicular to the main flow direction, respectively). We verified that u was the dominant velocity component since its average value was almost equal to the average of U and at least two orders of magnitude more than the v component average.

2.3 Data analysis

2.3.1 Colloid transport over the rock surface

To qualitatively show the colloid transport over the rock surface, we used the fluorescence images, captured at various times, and applied the following procedure. First, we converted the color images exported by the microscope's software to grayscale images. We then subtracted the background (time zero) image from the other images. Next, we used a global threshold to binarize the images and obtained a mask of the regions covered by the fluorescent colloids. Finally, we combined the binarized images at different times, to show the evolution of fluorescence in the flow cell with time.

2.3.2 Colloid breakthrough curves

We quantified the fluorescence emission intensity of eluent samples collected during the experiments using an Infinite 200 fluorescence plate reader (Tecan, Männedorf, Switzerland), using excitation and emission wavelengths of 500 and 560 nm, respectively. To prevent interference between the excitation light of the plate reader and the emitted light from the colloids, the excitation wavelength had to be lower than the optimal value of 540 nm. Nevertheless, due to the beads' high fluorescence intensity, this did not affect our observations. The fluorescence intensities of the eluent samples were compared to the intensity of the pulse suspension to obtain the relative concentration C/C_0, where C and C_0 are the specific sample and pulse concentrations, respectively.

We estimated the colloid mass recovery from the breakthrough curves by directly calculating the ratio between the total pulse fluorescence and the total eluted fluorescence. The total fluorescence of the pulse was calculated as

$$\Phi_{pulse} = \phi_{pulse} V_{pulse}, \quad (10)$$

where ϕ_{pulse} [arbitrary units] is the fluorescence measured in the pulse suspension, and V_{pulse} [L³] is the total volume of the pulse. The recovered fluorescence was calculated as

$$\Phi_{rec} = \sum \phi_i V_i, \quad (11)$$

where ϕ_i is the fluorescence measured in each eluted sample i, and V_i [L³] is the sample's volume. We then calculated the mass recovery as Φ_{rec}/Φ_{pulse}.

*2.3.3 **Residual colloid surface concentration***

To quantify the residual colloid concentration on the rock surface, we took fluorescence images of the surface at the end of the experiment (after the wash stage, see Section 2.1.4). To reduce the noise in the calculation, we averaged the fluorescence intensity in 10 × 10 pixels windows. Next, we used a calibration curve (see below) to transform the intensity values to surface colloid concentrations (colloid mass per rock surface area). Finally, we calculated the longitudinal concentration profiles by averaging along transects perpendicular to the flow direction,

$$\overline{C_s}(x) = \frac{1}{w} \int C_s(x, y) dy, \quad (12)$$

where C_s [ML⁻²] is the surface concentration, w [L] is the rock sample width, and x and y are the coordinates parallel and perpendicular to the flow direction, respectively.

To obtain the surface concentration calibration curve, we first placed a colloid suspension drop with a known concentration on the rock surface under the fluorescence microscope and measured the area of the fluorescent mark created on the surface. Using the known volume and concentration in the drop, we could determine the overall mass of colloids on the surface. We then calculated the colloids' overall surface mass concentration (in dimensions of [ML⁻²]). Next, we obtained a representative value of the fluorescence intensity per unit of rock surface area by averaging the intensity in 10 equally sized sub-regions of each mark. The calibration curve was then linearly fitted to the plot of surface concentrations and fluorescence intensity values.

2.3.4 *Longitudinal dispersion coefficients*

We calculated the longitudinal dispersion coefficients directly from the images, using the concentration field's first and second central spatial moments in the longitudinal direction (Detwiler et al., 2000). They represent the position of the center of mass of the colloid plume $M_1(x)$ [L] and its variation $M_2(x)$ [L^2]. We first subtracted the background image from the other images and then normalized them by the image with the maximum intensity. Following that, we thresholded the images to obtain the continuous colloid plume structure with the normalized concentration field C. We then calculated $M_1(x)$ and $M_2(x)$ as

$$M_1(x) = \frac{\sum_{i=1}^{nx}\sum_{j=1}^{ny} x_{ij}C_{ij}}{\sum_{i=1}^{nx}\sum_{j=1}^{ny} C_{ij}} \quad 13)$$

and

$$M_2(x) = \frac{\sum_{i=1}^{nx}\sum_{j=1}^{ny}\left(x_{ij} - M_1(x)\right)^2 C_{ij}}{\sum_{i=1}^{nx}\sum_{j=1}^{ny} C_{ij}}, \quad 14)$$

where nx and ny are the numbers of pixels in the longitudinal and transverse directions, i and j are the longitudinal and transverse coordinates, x_{ij} is the longitudinal position of each pixel, and C_{ij} is the normalized concentration in the pixel. During the early stage of the experiments $M_2(x)$ continuously increases until the colloid plume is spread over the entire field of view. The longitudinal dispersion coefficient D_L [L^2/T] was then calculated from this early-time evolution of M_2 as

$$D_L = \frac{1}{2}\frac{dM_2}{dt}. \quad 15)$$

Table 1. *Characteristics of the flow cells and the experimental conditions.*

Experiment name[a]	Typical fracture aperture b [cm]	Fracture aperture volume V_f [cm³]	Flow rate Q [cm³/min]	Mean flow velocity $\overline{u}$ [cm/min]	Re[b]	Pe[c]	D_L/D_0[d] $\pm$ standard error [-]
LH	0.15	6.16	0.1	0.167	0.0434	9.66×10^4	$3.27 \pm 0.86 \times 10^4$
LH-b	0.15	6.16	0.09	0.150	0.0390	8.68×10^4	$3.23 \pm 0.16 \times 10^4$
HH	0.094	4.74	0.1	0.266	0.0435	9.64×10^4	$4.45 \pm 0.83 \times 10^4$
HH-b	0.094	4.74	0.11	0.293	0.0477	10.62×10^4	$4.21 \pm 2.33 \times 10^4$

[a] – LH, LH-b: low heterogeneity rock surface; HH, HH-b: high heterogeneity rock surface. See Sections 2.1.2 and 2.1.4 for details.

[b] – Reynolds number, Eq. 4.

[c] – Péclet number, Eq. 3.

[d] – Longitudinal dispersion coefficient (Eq. 15) normalized by the diffusion coefficient, Eq. 5 and Section 2.2.1.

3 Results and discussion

3.1 Calculated fluid velocities

To link the fracture aperture distribution to colloids transport behavior, we show the COMSOL®-calculated velocity magnitudes over two fracture surfaces, a natural fracture surface (HH) and an artificial fracture surface (LH) (Fig. 2(c)). Velocities are expressed as the relative velocity $U(x,y)/\overline{U}$, where $U(x,y)$ and $\overline{U}$ are the local velocity magnitude and its average, respectively (see Section 2.2.2). The resulting $\overline{U}$ values matched the mean flow velocity $\overline{u}$ values reported in Table 1. The simulated flow velocities over the HH surface were non-uniform and preferential, with higher

velocities at locations of large aperture, as expected. In contrast, the velocities over the LH surface were more uniform. The velocities over the HH surface also showed a wider range of values compared to the LH surface, in agreement with the differences in aperture values distribution between the two surfaces (Fig. 2(b)).

Similar to previous works, we see how regions with higher aperture and higher transmissivity generally contribute to higher local velocities (Klepikova et al., 2021; Stoll et al., 2019), which is also expected from Eq. 6. We note that in our case, the orientation of the aperture field could be considered flow-enhancing (Méheust & Schmittbuhl, 2001) by creating a preferential flow channel. When the general orientation of the fracture surface topography variation is perpendicular to the main flow direction, the velocity field might not be trivially correlated to the spatial aperture variation (Huber et al., 2012). In addition, when the fracture width (the horizontal dimension perpendicular to the main flow direction) changes, for example, by regions of zero aperture, flow could be accelerated locally in regions of low aperture and transmissivity (Huber et al., 2012). Thus, it is important to understand the fracture aperture variation relative to the experimental conditions to correctly interpret the flow and transport behavior. Using roughness measurement coupled with direct visualization of the transport behavior, as we present here, is crucial to model transport phenomena at the single fracture scale. In addition, it was shown that the local cubic law (Eq. 6) could introduce significant errors in the estimation of local fluxes. To this end, Wang et al. (2015) proposed a modified local cubic law with a correction factor to account for inertia and local tortuosity effects in rough fracture flows. However, using the data given by Wang et al. (2015), we found this correction factor to be 1 for our HH surface apertures and our experimental Reynolds number. Thus, a correction for the local cubic law solution was unnecessary in our case.

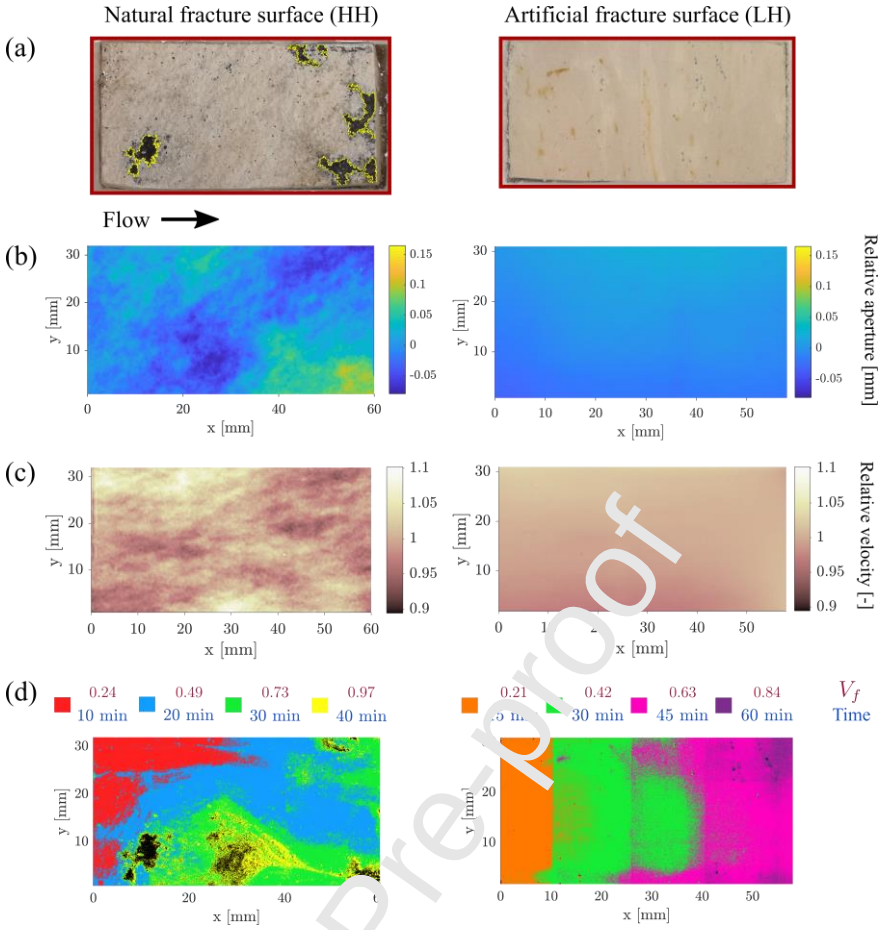

Figure 2. *(a) Color images of two rock surfaces used in this study: a natural fracture surface characterized by a high degree of heterogeneity (HH, left column) and an artificially created fracture surface from a non-fractured rock core (LH, right column). The natural fracture surface was characterized by large dark-colored patches, which we attributed to deposited minerals on the surface (see the regions outlined in yellow). The arrow indicates the flow direction. (b) The relative fracture apertures represent the difference between the local aperture value and its average, to highlight the higher aperture variability in the natural fracture surface. Note that the overall aperture variations were 0.11 and 0.24 mm for the LH and HH samples, respectively (see Section 2.1.2). (c) Calculated velocity magnitudes U normalized by their average $\bar{U}$ (see Section 3.1) over the natural and artificial fracture surfaces (left and right, respectively). High velocities are related to large aperture regions of the rock sample. (d) Higher fracture surface heterogeneity and velocity variation led to preferential colloid transport. We qualitatively show the plume of the fluorescent colloid cover over the natural and artificial fracture surfaces (left and right, respectively) at different times. The colors represent the time (or fracture aperture volume V_f) at which the colloid front covered different parts of the surface. Black color indicates regions not covered by fluorescence (observed only on the natural, partially coated surface). We used different time intervals for the two experiments due to the difference in flow velocities (see Table 1). We also note that the colloid front here is a qualitative measure intended to show the time evolution of the plume and does not represent a specific relative colloid concentration value. (For the interpretation of colors in the figure, the reader is referred to the web version of the article).*

3.2 Direct visualization of fluorescent colloid transport

We observed a strong impact of the fracture surface topography and velocity variation on the advancing colloid front for different surface heterogeneities under the same flow rate. With the natural fracture rock surface (experiment HH; Table 1), a preferential colloid transport path was created along the rock surface due to the variation in the fracture topography. On the other hand, the colloid front was relatively straight perpendicular to the flow direction with the artificially created rock surface (experiment LH; Table 1). In Fig. 2(d), we show the dynamics of colloid transport over the surface during the first part of the experiment until shortly after their breakthrough at the outlet.

Numerical simulations have previously shown the impact of fracture aperture heterogeneity on the transport of monodispersed, neutrally-buoyant colloids, similar to those used here. Higher fracture aperture correlation length in the flow direction, which also characterized our HH fracture surface, resulted in increased width of the transported particles front (Chrysikopoulos & James, 2003), which we confirm here experimentally. Moreover, simulations with polydisperse and dense particles have resulted in similar trends (Chrysikopoulos & James, 2003; Ding et al., 2021), indicating that our experimental results could be qualitatively relevant for other particle types.

The calculated effective longitudinal dispersion coefficients are shown in Table 1, normalized by the diffusion coefficient of the colloids (Eq. 5 and Section 2.2.1). As expected, the values for the HH and HH-b experiments were higher than the LH and LH-b experiments. Although these differences are not significant, the trend is consistent. This was evidently the result of the larger velocity variations in the HH and HH-b experiments (Fig. 2(c)). Our results are in good agreement with previous results by Detwiler et al. (2000), who calculated the dispersion coefficients for solutes in rough- and smooth-walled synthetic fractures. They found that the normalized dispersion coefficients in the rough-walled fracture were ~2 times larger than in the smooth-walled (Hele-Shaw) fractures for similar Pe numbers. Our experiments found a ratio of up to 1.78 between the normalized dispersion coefficients of the rough (HH and HH-b) and smooth (LH and LH-b) rock surfaces.

In some regions of the rock surface, we did not observe a significant fluorescent cover at the time of breakthrough or immediately after it. In these regions, fluorescence was apparent only in a few interspersed pixels, and thus, it was not

observed in the full image. These regions appear in black in Fig. 2(d), and they are most apparent for the high heterogeneity surface (HH). We mostly attribute this behavior to the heterogeneous velocity field that delayed the arrival of colloids to regions where the fracture aperture was narrower, and velocity was expected to decrease (Brown et al., 1998; Stoll et al., 2019). At later times, not shown in Fig. 2(d), the fluorescence over most of the rock surface increased, indicating that colloids eventually covered the entire surface. However, the reduced fluorescence is also attributed, in part, to the dark coating on some parts of the natural fracture surface (see the yellow-outlined regions in Fig. 2(a), left panel). While we could not verify this, the surface's dark color appeared to reduce the fluorescence intensity of colloids flowing over (or deposited on) it. Nevertheless, the coated areas accounted for only a part of the regions where fluorescence was low or late-arriving. Therefore, we maintain that preferential flow still significantly contributed to the earlier breakthrough of colloids in the natural fracture surface experiments and their late arrival in some regions.

3.3 Colloid breakthrough curves and mass recovery

We observed earlier colloid breakthrough with the natural fracture rock surfaces (experiments HH and HH-b; Table 1) than with the artificially created surfaces (experiments LH and LH-b; Table 1), as we show in Fig. 3. We attribute this behavior to the varied topography of the natural rock surfaces, which encouraged the emergence of preferential flow and colloid transport (see Fig. 2(c)-(d)). To determine the x-axis of Fig. 3, we multiplied the time by the flow rate and divided it by the total fracture aperture volume to obtain the number of fracture aperture volumes that passed through the flow cell.

To compare the breakthrough behavior between experiments, we found the number of fracture aperture volumes needed to reach the normalized concentration of C/C_0 = 0.5. In our experiments, the colloid breakthrough curves reached C/C_0 = 0.5 after 0.62 and 0.67 fracture aperture volumes for natural fracture rock surfaces (experiments HH-b and HH, respectively). With the artificially created fracture surfaces (experiments LH and LH-b), the number of fracture aperture volumes required to reach C/C_0 = 0.5 were 1.2 and 1.55 (experiments LH-b and LH, respectively). The small difference between the values for the two LH samples could have been the result of using different rock samples.

The differences between the values of the C/C_0 fracture aperture volumes for the LH and HH samples show the impact of preferential flow developed along the heterogenous natural fracture surface on the early breakthrough of the colloids. These values also agree with the qualitative images showing earlier colloids' breakthrough in the natural fracture surface experiments (Fig. 2(d)). In addition, the breakthrough curves from the HH and HH-b experiments are less symmetric, showing the signature of anomalous transport (Berkowitz & Scher, 1997). Breakthrough curves for monodisperse colloids have also shown that increasing the aperture correlation length in the flow direction can lead to earlier colloid breakthrough compared to an isotropic fracture surface (Chrysikopoulos & James, 2003). Thus, our experimental observations agree with earlier numerical results.

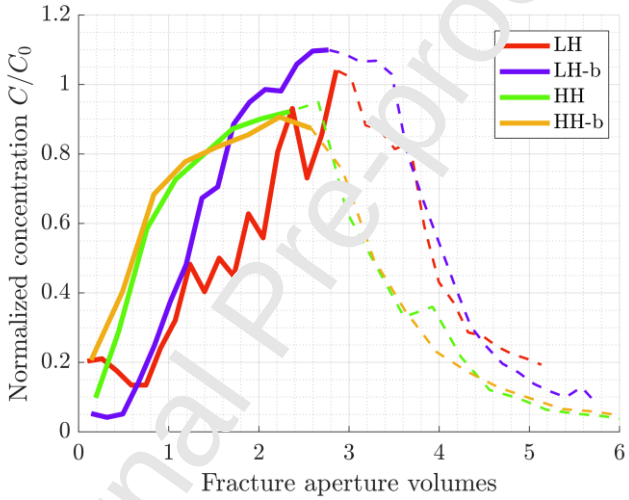

Figure 3. *The colloid breakthrough curves show the preferential transport of colloids along the natural fracture surface. Breakthrough curves are plotted as the outflow colloid concentration divided by the initial pulse concentration (C/C_0) for experiments with an artificially created rock surface (LH and LH-b) and a natural fracture surface (HH and HH-b). The breakthrough curves are plotted against the number of fracture aperture volumes passed through the cell. The solid part of the lines represents the pulse duration, and the dashed part represents the wash with the background solution. (For the interpretation of colors in the figure, the reader is referred to the web version of the article).*

The recovery values $\Phi_{rec}/\Phi_{pulse}\times100$ [%] we obtained were 89.2, 107.9, 87.3, and 102.2%, respectively, for experiments LH, LH-b, HH, and HH-b. We could not find a trend between the mass recovery values and the sample type, but this could have been the result of the limited number of experiments. We note that recovery values of >100% are not physically possible and probably result from the accumulation of inaccuracy of the fluorescence measurements.

We note that the number of experiments presented here is quite limited, with two experiments per each fracture surface type. However, we observed a clear trend of the impact of fracture surface topography on colloid transport behavior in our experiments, and this trend was consistent within our results. Thus, we found these results to be reliable and plausible, as well as representative of the colloids' expected transport behavior.

3.4 Surface heterogeneity and colloid deposition

The longitudinal profiles of residual colloid concentrations on the rock surface at the end of the experiment were determined from fluorescence images of the rock surface at the end of the experiments' washing stage (see Section 2.1.4). The fluorescence intensity was transformed to surface concentration using the calibration curve described in Section 2.3.3. The residual colloid concentration profiles exhibited higher concentrations close to the inlet, which decreased along the flow direction (Fig. 4). A similar surface concentration profile was shown in colloid transport simulations by James & Chrysikopoulos (1999). The enhanced retention of colloids near the inlet was also shown experimentally in a parallel-plate flow cell with a treated quartz surface. This non-linear trend of enhanced particle retention was mostly attributed to hydrodynamic flow effects, which impacted the flux of colloids to the rough surface (Jin et al., 2015). In addition, we did not observe a notable difference in the residual colloid deposition between the two surface types, although the natural fracture surface (HH) was characterized by a slightly higher roughness than the artificially created fracture surface (LH). We calculated Ra = 11.5 and 26.3 μm, and Rq = 14.0 and 33.5 μm for the LH and HH surfaces, respectively. These roughness values were determined over a surface of ~2500 mm^2 and may not represent the nanoscale roughness, which is often associated with the colloid retention mechanisms (Rasmuson et al., 2019; Stoll et al., 2016). However, the similarity in these profiles may suggest that the nanoscale roughness did not impact colloid deposition in our experiments. In the LH experiment, we also observed an increase in concentration near the outlet. This may have been an artifact related to hydrodynamic edge effects, in which the flow profile changed due to the transition from the rock surface to the enclosing flow cell structure and the thin layer of PDMS used to seal the rock sample in place (see Section 2.1.1). A narrower flow profile near the cell outlet might have led to the compression of the flow lines in the vertical direction and increased colloid

deposition. While this change in the flow regime could have affected the overall colloid transport behavior near the outlet, we could not see this impact in the images.

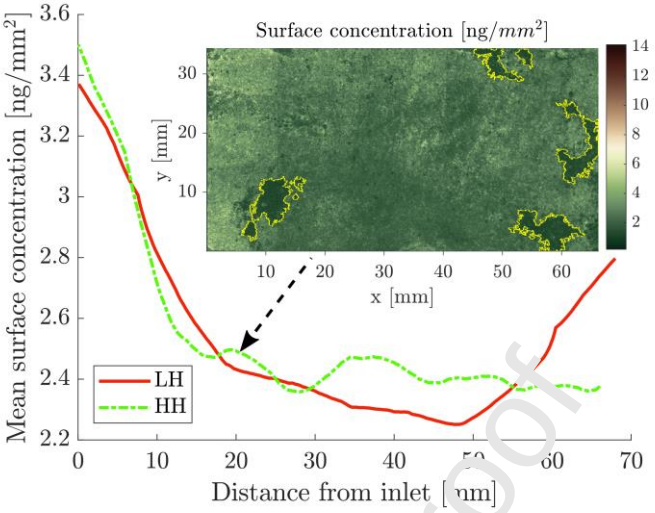

Figure 4. *Surface concentration profiles of the colloids at the end of the experiments for artificially created (LH) and natural fracture (HH) surfaces. The inset shows an image of the natural fracture surface at the end of the experiment, highlighting regions of apparently very low colloid deposition in dark green, measured from the fluorescence intensity. The regions delimited by the yellow lines correspond to the yellow-delimited regions in Fig. 2(a). (For the interpretation of colors in the figure, the reader is referred to the web version of the article).*

In the inset of Fig. 4, we show the residual surface concentration of colloids over the natural fracture surface (at the end of the HH experiment) and reveal another interesting result. We observed regions on the surface with apparently very low residual concentrations of fluorescent colloids (appearing in dark green in the inset). This observation could be attributed either to the surface's chemical heterogeneity or to the variations in the flow field, as we explain below. First, the low fluorescence regions appear to be related to deposited minerals on the rock surface (black coating in Fig. 2(a)). However, as we see in Fig. 2(d) and subsequent images not shown here, these regions remained relatively darker throughout the experiment, even at later times when we expected the colloids to reach low-velocity zones and cover the entire surface. Therefore, while this low fluorescence could be attributed to low concentrations of deposited colloids, it could also be attributed to a reduction in fluorescence intensity by the darker background.

While we could not determine whether dark-coated rock surface regions contributed to reduced deposition, discussing the chemical differences between the rock surfaces is still interesting. We performed SEM-EDS measurements of several

samples from the bulk rock and the natural fracture surfaces. The elemental analysis of the bulk rock samples showed the presence of Ca, Si, P, O, and C, suggesting that the artificially created surface was composed of calcium carbonates, calcium phosphates, and silicates. The analysis of the natural fracture surface additionally showed the presence of Mn, Ni, Fe, Al, and Mg, suggesting that manganese and nickel oxides and clay minerals coated the rock surface. These elements were also observed on the surfaces of natural coated fracture surfaces in chalk in previous studies (Weisbrod et al., 1999).

Since manganese oxides were expected to have ζ-potentials in the range of -20 to -30 mV at the experimental pH of ~6.5 (Zhang et al., 2017), they might have repelled the synthetic colloids, whose measured ζ-potential is -58 mV. However, since the ζ-potential of crushed-chalk powder, representing the pristine rock surface, is also negative at a pH of approximately 7 (-20 mV; Zvikelsky et al., 2008), electrostatic repulsion alone may not explain the reduced deposition of colloids on the coated surface patches. In addition, the ζ-potential of crushed rock does not always represent the value on a fracture surface made of the same material (Song et al., 2017). We note that the ζ-potential alone cannot determine the tendency for increased or reduced colloid retention, and hydrodynamic effects and surface charge heterogeneity are also important factors (Jin et al., 2015; Rasmuson et al., 2019; Ron et al., 2019). Extended DLVO theory (van Oss, 2006) calculations, using the Parti-Suite software (https://wpjohnsongroup.utah.edu/trajectoryCodes.html), showed that increasing the nanoscale roughness length, as expressed by the height of the asperities, relative to the mean surface, from 10 and 100 nm resulted in a ~10-fold increase in the minimum total interaction energy profile, which would limit colloid retention. Finally, the ζ-potential of glass under our experimental conditions (ionic strength and pH) is expected to be <-60mV (Gu & Li, 2000). Therefore, we did not expect the surface charge of the glass cover to impact the overall flow and deposition of colloids in the cell.

4 Summary and conclusions

This work described an original experimental setup that allowed for direct visualization of colloid transport over a natural and artificial rock fracture surface. We used this setup to perform colloid transport experiments with two types of chalk rock surfaces: (1) an artificially created fracture surface that exhibited lower physical heterogeneity and similar mineralogical composition to the bulk rock; and (2) a

natural (active) fracture surface taken from a core drilled below the water table in the Israeli Negev Desert. The latter surface exhibited varying fracture aperture alterations and surface mineralogical composition. We show that aperture variation can create preferential colloid transport paths, or channeling, over the rock surface. We further show how the preferential transport pathways translated into an earlier emergence of colloids by measuring their breakthrough curves. Finally, we were able to show experimentally that dispersion coefficients with natural fracture surfaces were twice those of smooth fracture surfaces. Thus, natural rock samples demonstrate similar trends to those observed with synthetic fractures (Detwiler et al. 2000), further strengthening the validity of our method.

While we observed the surface geometry's impact on colloid transport and dispersion, we did not see a great impact of the varying surface mineralogy on colloid deposition and retention. This could have been due to similarities in the nanoscale heterogeneity between the surfaces, which is crucial for colloid retention (e.g., Rasmuson et al., 2019) and which we were not able to estimate. Nevertheless, our experimental system enabled us to directly quantify colloid dispersion, a key factor in upscaled transport models of fractured media, which is not readily quantifiable from nanoscale systems. It is also possible that different types of colloids, with varying surface properties, different densities and/or different sizes, would have given different results.

While some of our findings were previously reported by others (Chrysikopoulos & James, 2003; Detwiler et al., 2000; Méheust & Schmittbuhl, 2000; Rodrigues & Dickson, 2015; Stoll et al., 2016), our work is unique in several aspects. Most of all, it brings together direct observations of colloid transport and breakthrough curves analysis in a single setup, using natural rough fracture surfaces. More specifically, most studies on the impact of fracture surface roughness on colloid transport used numerical methods (Boutt et al., 2006; Chrysikopoulos & James, 2003; Ding et al., 2021; Huber et al., 2012; James et al., 2018; Klepikova et al., 2021). These works are fundamental to our understanding of flow and colloid transport in rough fractures and lay the theoretical basis for interpreting and predicting these phenomena. However, experimental work is necessary to ground numerical models' findings and help uncover new and unexpected behavior and improve model reliability. In addition, it is essential to design and carry out experiments that directly show basic flow and transport mechanisms, not only treat them as a "black box" (Huber et al., 2012). At the

same time, numerical simulations can overcome some experimental limitations, most notably the difficulty of realizing many different samples, which is more apparent when studying the impact of heterogeneity (Borgman et al., 2019). Thus, it is crucial to advance in both channels, and this work contributes to the development of experimental methods for fracture flow and transport exploration and quantification.

We managed to understand better and quantify the differences between flow and transport processes along natural versus artificial fracture surfaces using a new visualization experimental setup combined with data analyses. Future applications of this method could, for example, further explore the impact of different flow conditions by varying the Péclet numbers and varying colloid adsorption affinity by using surface-modified particles. The possible use of modified fluorescent clay particles (e.g., Diaz et al., 2013) could also be considered, further enhancing the ability to experiment with more environmentally-relevant colloids.

Acknowledgments

This work was funded by the Israel Science Foundation, under grant no. 165/17. We thank Dr. Ana Millionshchick from the Ilse Katz Institute for Nanoscale Science & Technology in the Ben-Gurion University of the Negev for the SEM-EDS analyses. OB acknowledges the generous support of the Ben-Gurion University of the Negev through the Marcus Postdoctoral Fellowship in Water Sciences, and thanks Emily Tran for helpful discussions. The data used to generate the figures in this paper can be found at doi:10.5281/zenodo.6334815.

Author statement

Oshri Borgman: Conceptualization, Methodology, Investigation, Writing - Original Draft, Visualization. **Avraham Be'er:** Conceptualization, Methodology, Resources, Writing - Review & Editing, Supervision. **Noam Weisbrod:** Conceptualization, Resources, Writing - Review & Editing, Supervision, Project administration, Funding acquisition.

Declaration of interests

The authors declare that they have no known competing financial interests or personal relationships that could have appeared to influence the work reported in this paper.

The authors declare the following financial interests/personal relationships which may be considered as potential competing interests:

References

Albarran, N., Missana, T., Alonso, U., García-Gutiérrez, M., & López, T. (2013). Analysis of latex, gold and smectite colloid transport and retention in artificial fractures in crystalline rock. *Colloids and Surfaces A: Physicochemical and Engineering Aspects*, *435*, 115–126. doi: 10.1016/j.colsurfa.2013.02.002

Alonso, U., Missana, T., Patelli, A., Ceccato, D., Albarran, N., García-Gutiérrez, M., ... Rigato, V. (2009). Quantification of Au nanoparticles retention on a heterogeneous rock surface. *Colloids and Surfaces A: Physicochemical and Engineering Aspects*, *347*(1-3), 230–238. doi: 10.1016/j.colsurfa.2009.04.046

Becker, M. W., Reimus, P. W., & Vilks, P. (1999). Transport and attenuation of carboxylate-modified latex microspheres in fractured rock laboratory and field tracer tests. *Ground Water*, *37*(3), 387–395. doi: 10.1111/j.1745-6584.1999.tb01116.x

Berkowitz, B. (2002). Characterizing flow and transport in fractured geological media: A review. *Advances in Water Resources*, *25*(8-12), 861–884. doi: 10.1016/S0309-1708(02)00042-8

Berkowitz, B., & Scher, H. (1997). Anomalous Transport in Random Fracture Networks. *Physical Review Letters*, *79*(20), 4038–4041. doi: 10.1103/PhysRevLett.79.4038

Berre, I., Doster, F., & Keilegavlen, E. (2019). Flow in Fractured Porous Media: A Review of Conceptual Models and Discretization Approaches. *Transport in Porous Media*, 130(1), 215–236. doi: 10.1007/s11242-018-1171-6

Bird, R. B., Stewart, W. E., and Lightfoot, E. N., *Transport phenomena*, 2nd ed. New York: John Wiley and Sons, Inc., 2002.

Bodin, J., Delay, F., & de Marsily, G. (2003). Solute transport in a single fracture with negligible matrix permeability: 1. fundamental mechanisms. *Hydrogeology Journal*, *11*(4), 418–433. doi: 10.1007/s10040-003-0268-2

Borgman, O., Darwent, T., Segre, E., Goehring, L., Holtzman, R., (2019). Immiscible fluid displacement in porous media with spatially correlated particle sizes. *Advances in Water Resources, 128*, 158–167. doi: 10.1016/j.advwatres.2019.04.015

Boutt, D. F., Grasselli, G., Fredrich, J. T., Cook, B. K., & Williams, J. R. (2006). Trapping zones: The effect of fracture roughness on the directional anisotropy of fluid

flow and colloid transport in a single fracture. *Geophysical Research Letters*, *33*(21), L21402. doi: 10.1029/2006GL027275

Brewer, A., Dror, I., & Berkowitz, B. (2021). The Mobility of Plastic Nanoparticles in Aqueous and Soil Environments: A Critical Review. *ACS ES&T Water*, *1*(1), 48–57. doi: 10.1021/acsestwater.0c00130

Brown, S., Caprihan, A., & Hardy, R. (1998). Experimental observation of fluid flow channels in a single fracture. *Journal of Geophysical Research: Solid Earth*, *103*(B3), 5125–5132. doi: 10.1029/97JB03542

Chinju, H., Kuno, Y., Nagasaki, S., & Tanaka, S. (2001). Deposition behavior of polystyrene latex particles on solid surfaces during migration through an artificial fracture in a granite rock sample. *Journal of Nuclear Science and Technology*, *38*(6), 439–443. doi: 10.1080/18811248.2001.9715051

Chrysikopoulos, C. V., & James, S. C. (2003). Transport of neutrally buoyant and dense variably sized colloids in a two-dimensional fracture with anisotropic aperture. *Transport in Porous Media*, *51*(2), 191–210. doi: 10.1023/A:1021952226861

Cohen, M., & Weisbrod, N. (2018). Field scale mobility and transport manipulation of carbon-supported nanoscale zerovalent iron in fractured media. *Environmental Science and Technology*, *52*(14), 7849–7858. doi: 10.1021/acs.est.8b01226

de Anna, P., Dentz, M., Tartakovsky, A., & Le Borgne, T. (2014). The filamentary structure of mixing fronts and its control on reaction kinetics in porous media flows. *Geophysical Research Letters*, *41*(13), 4586–4593. doi: 10.1002/2014GL060068

Detwiler, R. L., Rajaram, H., & Glass, R. J. (2000). Solute transport in variable-aperture fractures: An investigation of the relative importance of Taylor dispersion and macrodispersion. *Water Resources Research*, 36(7), 1611–1625. doi: 10.1029/2000WR900036

Diaz, C. A., Xia, Y., Rubino, M., Auras, R., Jayaraman, K., & Hotchkiss, J. (2013). Fluorescent labeling and tracking of nanoclay. *Nanoscale*, *5*(1), 164–168. doi: 10.1039/c2nr32978f

Ding, Y., Meng, X., & Yang, D. (2021). Numerical simulation of polydisperse dense particles transport in a random-orientated fracture with spatially variable apertures.

Colloids and Surfaces A: Physicochemical and Engineering Aspects, *610*, 125729. doi: 10.1016/j.colsurfa.2020.125729

Froidevaux, P., Steinmann, P., & Pourcelot, L. (2010). Long-term and long-range migration of radioactive fallout in a karst system. *Environmental Science and Technology*, *44*(22), 8479–8484. doi: 10.1021/es100954h

Gramling, C. M., Harvey, C. F., & Meigs, L. C. (2002). Reactive Transport in Porous Media: A Comparison of Model Prediction with Laboratory Visualization. *Environmental Science and Technology*, *36*(11), 2508–2514. doi: 10.1021/es0157144

Gu, Y., & Li, D. (2000). The ζ-potential of glass surface in contact with aqueous solutions. *Journal of Colloid and Interface Science*, *226*(2), 328–339. doi: 10.1006/jcis.2000.6827

Horton, A. A., & Dixon, S. J. (2018). Microplastics: An introduction to environmental transport processes. *Wiley Interdisciplinary Reviews: Water*, *5*(2), e1268. doi: 10.1002/wat2.1268

Hu, R., Zhou, C. X., Wu, D. S., Yang, Z., & Chen, Y. F. (2019). Roughness Control on Multiphase Flow in Rock Fractures. Geophysical Research Letters, 46(21), 12002–12011. doi: 10.1029/2019GL084762

Huber, F., Enzmann, F., Wenka, A., Bouby, M., Dentz, M., & Schäfer, T. (2012). Natural micro-scale heterogeneity induced solute and nanoparticle retardation in fractured crystalline rock. *Journal of Contaminant Hydrology*, *133*, 40–52. doi: 10.1016/J.JCONHYD.2012.03.004

Ishido, T., & Mizutani, J. (1981). Experimental and theoretical basis of electrokinetic phenomena in rock-water systems and its applications to geophysics. Journal of Geophysical Research, 86(B3), 1763–1775. doi: 10.1029/JB086IB03P01763

James, S. C., & Chrysikopoulos, C. V. (1999). Transport of polydisperse colloid suspensions in a single fracture. *Water Resources Research*, 35(3), 707–718. doi: 10.1029/1998WR900059

James, S. C., & Chrysikopoulos, C. V. (2003). Effective velocity and effective dispersion coefficient for finite-sized particles flowing in a uniform fracture. *Journal of Colloid and Interface Science*, *263*(1), 288–295. doi: 10.1016/S0021-9797(03)00254-6

James, S. C., Wang, L., & Chrysikopoulos, C. V. (2018). Modeling colloid transport in fractures with spatially variable aperture and surface attachment. *Journal of Hydrology*, *566*, 735–742. doi: 10.1016/j.jhydrol.2018.09.047

Jin, C., Glawdel, T., Ren, C. L., & Emelko, M. B. (2015). Non-linear, non-monotonic effect of nano-scale roughness on particle deposition in absence of an energy barrier: Experiments and modeling. *Scientific Reports*, *5*(1), 1–14. doi: 10.1038/srep17747

Kang, P. K., Dentz, M., Le Borgne, T., Juanes, R., (2015). Anomalous transport on regular fracture networks: Impact of conductivity heterogeneity and mixing at fracture intersections. *Physical Review E*, *92*(2), 022148. doi: 10.1103/PhysRevE.92.022148

Kersting, A. B., Efurd, D. W., Finnegan, D. L., Rokop, D. J., Smith, D. K., & Thompson, J. L. (1999). Migration of plutonium in ground water at the Nevada Test Site. *Nature*, *397*(6714), 56–59. doi: 10.1038/16231

Klepikova, M., Méheust, Y., Roques, C., & Linde, N. (2021). Heat transport by flow through rough rock fractures: a numerical investigation. *Advances in Water Resources*, 156, 104042. doi: 10.1016/J.ADVWATRES.2021.104042

Kurra, S., Hifzur Rahman, N., Regalla, S. P., & Gupta, A. K. (2015). Modeling and optimization of surface roughness in single point incremental forming process. *Journal of Materials Research and Technology*, *4*(3), 304–313. doi: 10.1016/j.jmrt.2015.01.003

Kurtzman, D., Nativ, R., & Adar, E. M. (2007). Flow and transport predictions during multi-borehole tests in fractured chalk using discrete fracture network models. *Hydrogeology Journal*, *15*(8), 1629–1642. doi:10.1007/s10040-007-0205-x

McCarthy, J. F., & Zachara, J. M. (1989). Subsurface transport of contaminants: binding to mobile and immobile phases in groundwater aquifers. *Environmental Science and Technology*, *23*(5), 496–502. doi: 10.1021/es00063a001

Medici, G., West, L. J., & Banwart, S. A. (2019). Groundwater flow velocities in a fractured carbonate aquifer-type: Implications for contaminant transport. *Journal of Contaminant Hydrology*, *222*, 1–16. doi: 10.1016/j.jconhyd.2019.02.001

Méheust, Y., & Schmittbuhl, J. (2000). Flow enhancement of a rough fracture. *Geophysical Research Letters*, *27*(18), 2989–2992. doi: 10.1029/1999GL008464

Méheust, Y., & Schmittbuhl, J. (2001). Geometrical heterogeneities and permeability anisotropy of rough fractures. *Journal of Geophysical Research: Solid Earth*, *106*(B2), 2089–2102. doi: 10.1029/2000jb900306

Missana, T., Alonso, U., García-Gutiérrez, M., & Mingarro, M. (2008). Role of bentonite colloids on europium and plutonium migration in a granite fracture. *Applied Geochemistry*, *23*(6), 1484–1497. doi: 10.1016/j.apgeochem.2008.01.008

Mondal, P. K., & Sleep, B. E. (2012). Colloid transport in dolomite rock fractures: Effects of fracture characteristics, specific discharge, and ionic strength. *Environmental Science and Technology*, *46*(18), 9987–9994. doi: 10.1021/es301721f

Nativ, R., Adar, E., & Becker, A. (1999). Designing a monitoring network for contaminated ground water in fractured chalk. *Ground Water*, 37(1), 38–47. doi: 10.1111/j.1745-6584.1999.tb00956.x

Neuweiler, I., Sorensen, I., & Kinzelbach, W. (2004). Experimental and theoretical investigations of drainage in horizontal rough-walled fractures with different correlation structures. Advances in Water Resources, 27(12), 1217–1231. doi: 10.1016/j.advwatres.2004.07.005

Noiriel, C., Madé, B., & Gouze, P. (2007). Impact of coating development on the hydraulic and transport properties in argillaceous limestone fracture. *Water Resources Research*, 43(9). doi: 10.1029/2006WR005379

Rasmuson, A., Pazmino, E., Assemi, S., & Johnson, W. P. (2017). Contribution of nano- to microscale roughness to heterogeneity: Closing the gap between unfavorable and favorable colloid attachment conditions. *Environmental Science and Technology*, *51*(4), 2151–2160. doi: 10.1021/acs.est.6b05911

Rasmuson, A., VanNess, K., Ron, C. A., & Johnson, W. P. (2019). Hydrodynamic versus Surface Interaction Impacts of Roughness in Closing the Gap between Favorable and Unfavorable Colloid Transport Conditions. *Environmental Science & Technology*, 53(5), 2450–2459. doi: 10.1021/acs.est.8b06162

Ron, C. A., Vanness, K., Rasmuson, A., & Johnson, W. P. (2019). How nanoscale surface heterogeneity impacts transport of nano- to micro-particles on surfaces under unfavorable attachment conditions. *Environmental Science: Nano*, 6(6), 1921–1931. doi: 10.1039/c9en00306a

Ron, C. A., & Johnson, W. P. (2020). Complementary colloid and collector nanoscale heterogeneity explains microparticle retention under unfavorable conditions. *Environmental Science: Nano*, 7(12), 4010–4021. doi: 10.1039/D0EN00815J

Rodrigues, S. N., & Dickson, S. E. (2015). The Effect of Matrix Properties and Preferential Pathways on the Transport of Escherichia coli RS2-GFP in Single, Saturated, Variable-Aperture Fractures. *Environmental Science and Technology*, *49*(14), 8425–8431. doi: 10.1021/acs.est.5b01578

Sahimi, M. (2011). *Flow and Transport in Porous Media and Fractured Rock*. Weinheim, Germany: Wiley-VCH Verlag GmbH & Co. KGaA. doi: 10.1002/9783527636693

Song, J., Zeng, Y., Wang, L., Duan, X., Puerto, M., Chapman, W. G., et al. (2017). Surface complexation modeling of calcite zeta potential measurements in brines with mixed potential determining ions (Ca2+, CO32−, Mg2+, SO42−) for characterizing carbonate wettability. *Journal of Colloid and Interface Science*, 506, 169–179. doi: 10.1016/J.JCIS.2017.06.096

Spanik, S., Rrokaj, E., Mondal, P. K., & Sleep, B. E. (2021). Favorable and unfavorable attachment of colloids in a discrete sandstone fracture. *Journal of Contaminant Hydrology*, *243*, 103919. doi: 10.1016/j.jconhyd.2021.103919

Stoll, M., Huber, F., Darbha, G., Schill, E., & Schäfer, T. (2016). Impact of gravity, collector surface roughness and fracture orientation on colloid retention kinetics in an artificial fracture. *Journal of Colloid and Interface Science*, *475*, 171– 183. doi: 10.1016/j.jcis.2016.04.045

Stoll, M., Huber, F., Trumm, M., Enzmann, F., Meinel, D., Wenka, A., ... Schäfer, T. (2019). Experimental and numerical investigations on the effect of fracture geometry and fracture aperture distribution on flow and solute transport in natural fractures. *Journal of Contaminant Hydrology*, *221*, 82–97. doi: 10.1016/j.jconhyd.2018.11.008

Tang, X.-Y., & Weisbrod, N. (2010). Dissolved and colloidal transport of cesium in natural discrete fractures. *Journal of Environmental Quality*, *39*(3), 1066–1076. doi: 10.2134/jeq2009.0345

Thoma, S. G., Gallegos, D. P., & Smith, D. M. (1992). Impact of fracture coatings on fracture/matrix flow interactions in unsaturated, porous media. *Water Resources Research*, *28*(5), 1357–1367. doi: 10.1029/92WR00167

Tran, E. L., Reimus, P., Klein-BenDavid, O., Teutsch, N., Zavarin, M., Kersting, A. B., & Weisbrod, N. (2020). Mobility of radionuclides in fractured carbonate rocks: Lessons from a field-scale transport experiment. *Environmental Science and Technology*, *54*(18), 11249–11257. doi: 10.1021/acs.est.0c03008

Trauscht, J., Pazmino, E., & Johnson, W. P. (2015). Prediction of Nanoparticle and Colloid Attachment on Unfavorable Mineral Surfaces Using Representative Discrete Heterogeneity. Langmuir, 31(34), 9366–9378. doi: 10.1021/acs.langmuir.5b02369

Tsang, C.-f., & Neretnieks, I. (1998). Flow channeling in heterogeneous fractured rocks. *Reviews of Geophysics*, *36*(2), 275–298. doi: 10.1029/97RG03319

Valocchi, A. J., Bolster, D., & Werth, C. J. (2019). Mixing-Limited Reactions in Porous Media. *Transport in Porous Media*, *130*(1), 157–182. doi: 10.1007/s11242-018-1204-1

van Oss, C. J. (2008). Chapter Three The Extended DLVO Theory. Interface Science and Technology, 16, 31–48. doi: 10.1016/S1573-4285(08)00203-2

Vilks, P., & Bachinski, D. B. (1996). Colloid and suspended particle migration experiments in a granite fracture. *Journal of Contaminant Hydrology*, *21*(1–4), 269–279. doi: 10.1016/0169-7722(95)00053-4

Wang, L., & Cardenas, M. B. (2014). Non-Fickian transport through two-dimensional rough fractures: Assessment and prediction. Water Resources Research, 50(2), 871–884. doi: 10.1002/2013WR014459

Wang, L., Cardenas, M. B., Slottke, D. T., Ketcham, R. A., & Sharp, J. M. (2015). Modification of the Local Cubic Law of fracture flow for weak inertia, tortuosity, and roughness. *Water Resources Research*, *51*(4), 2064–2080. doi: 10.1002/2014WR015815

Weisbrod, N., Meron, H., Walker, S., & Gitis, V. (2013). Virus transport in a discrete fracture. *Water Research*, *47*(5), 1888–1898. doi: 10.1016/j.watres.2013.01.009

Weisbrod, N., Nativ, R., Adar, E. M., & Ronen, D. (1999). Impact of intermittent rainwater and wastewater flow on coated and uncoated fractures in chalk. *Water Resources Research*, *35*(11), 3211–3222. doi: 10.1029/1999WR900194

Weisbrod, N., Nativ, R., Adar, E. M., Ronen, D., & Ben-Nun, A. (2000). Impact of coating and weathering on the properties of chalk fracture surfaces. *Journal of Geophysical Research: Solid Earth*, *105*(B12), 27853–27864. doi: 10.1029/2000jb900295

Yoon, S., & Kang, P. K. (2021). Mixing-Induced Bimolecular Reactive Transport in Rough Channel Flows: Pore-Scale Simulation and Stochastic Upscaling. *Transport in Porous Media*, 1–22. doi: 10.1007/S11242-021-01662-7/FIGURES/12

Zavarin, M., Roberts, S. K., Johnson, M. R., Hu, Q., Powell, B. A., Zhao, P., ... Pletcher, R. J. (2013). *Colloid-facilitated radionuclide transport in fractured carbonate rock from Yucca Flat, Nevada National Security Site* (Tech. Rep.). Livermore, California: Lawrence Livermore National Laboratory.

Zhang, H., Wu, A., Fu, H., Zhang, L., Liu, H., Zheng, S., ... Xu, Z. (2017). Efficient removal of Pb(ii) ions using manganese oxides: the role of crystal structure. *RSC Advances*, *7*(65), 41228–41240. doi: 10.1039/C7RA05955H

Zimmerman, R. W., & Bodvarsson, G. S. (1996). Hydraulic conductivity of rock fractures. *Transport in Porous Media*, *23*(1), 1–30. doi: 10.1007/BF00145263

Zvikelsky, O., & Weisbrod, N. (2006). Impact of particle size on colloid transport in discrete fractures. *Water Resources Research*, *42*(12), W12S08. doi: 10.1029/2006WR004873

Zvikelsky, O., Weisbrod, N., & Dody, A. (2008). A comparison of clay colloid and artificial microsphere transport in natural discrete fractures. *Journal of Colloid and Interface Science*, *323*(2), 286–292. doi: 10.1016/J.JCIS.2008.04.035

Highlights

- Colloid transport experiments with heterogeneous and smooth rock fracture surfaces
- Fluorescence visualization of colloid transport related to their breakthrough curves

- Heterogeneous surface leads to preferential flow compared with the smooth surface
- Preferential flow leads to earlier breakthroughs and higher dispersion coefficients
- Dispersion coefficients show trends similar to experiments with synthetic fractures